Title

Hybrid Li-Ion and Li-O2 Battery Enabled by Oxyhalogen-Sulfur Electrochemistry

Journal

Joule, 2(11)

ISSN

2542-4351

Authors

Wang, Xuefeng
Li, Yejing
Bi, Xuanxuan
et al.

Publication Date

2018-11-01

DOI

10.1016/j.joule.2018.07.019

Peer reviewed

Joule

CellPress

Article

Hybrid Li-Ion and Li-O_2 Battery Enabled by Oxyhalogen-Sulfur Electrochemistry

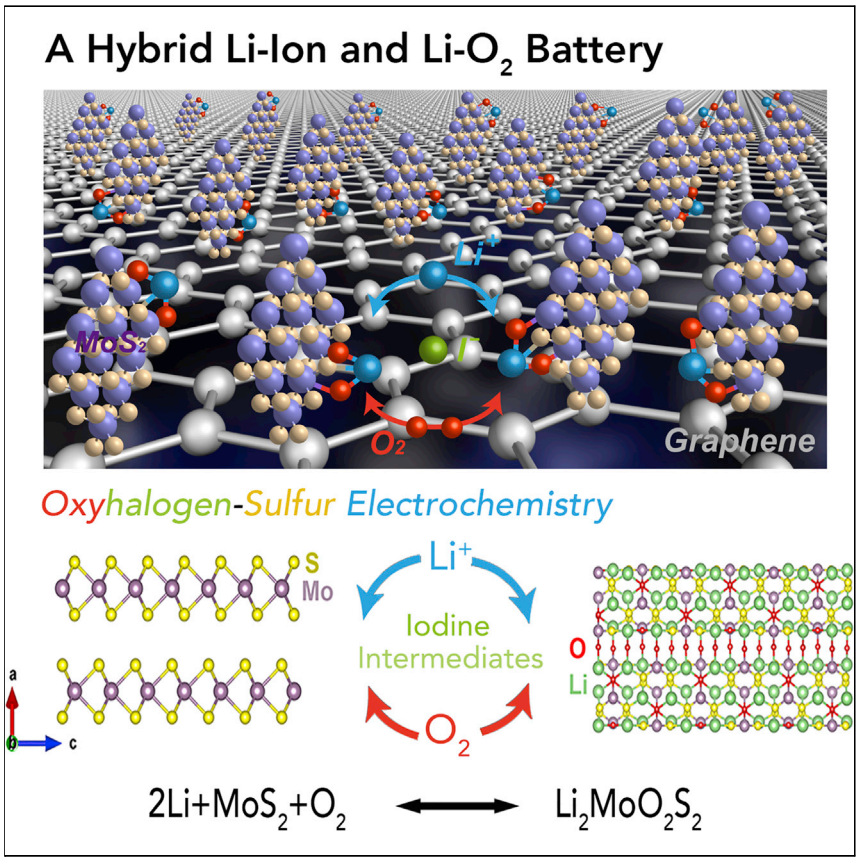

A hybrid Li-ion/Li-O_2 battery was constructed based on oxyhalogen-sulfur electrochemistry. Both Li ions and O anions can be reversibly stored in the MoS_2 structure, forming a $Li_2MoO_2S_2$ compound. This hybrid Li-ion/Li-O_2 cell combines the advantages of Li-ion and Li-O_2 batteries, which paves a way to push the limit of current Li-ion batteries and transition to the next generation of high-energy batteries.

Xuefeng Wang, Yejing Li, Xuanxuan Bi, ..., Khalil Amine, Jun Lu, Ying Shirley Meng

junlu@anl.gov (J.L.)
shirleymeng@ucsd.edu (Y.S.M.)

HIGHLIGHTS

Oxyhalogen-sulfur electrochemistry helps to build a hybrid Li-ion/Li-O_2 battery

Both Li ions and O anions can be reversibly stored in the MoS_2 structure

The $Li_2MoO_2S_2$ is isostructural to the Li_2MoO_4 rather than other thiomolybdates

Wang et al., Joule 2, 1–12
November 21, 2018
https://doi.org/10.1016/j.joule.2018.07.019

Please cite this article in press as: Wang et al., Hybrid Li-Ion and Li-O_2 Battery Enabled by Oxyhalogen-Sulfur Electrochemistry, Joule (2018), https://doi.org/10.1016/j.joule.2018.07.019

Joule

CellPress

Article

Hybrid Li-Ion and Li-O_2 Battery Enabled by Oxyhalogen-Sulfur Electrochemistry

Xuefeng Wang,[1] Yejing Li,[1] Xuanxuan Bi,[2] Lu Ma,[3] Tianpin Wu,[3] Mahsa Sina,[1] Shen Wang,[1] Minghao Zhang,[1,4] Judith Alvarado,[1,4] Bingyu Lu,[1] Abhik Banerjee,[1] Khalil Amine,[2] Jun Lu,[2,*] and Ying Shirley Meng[1,4,5,*]

SUMMARY

The large voltage hysteresis between charge and discharge results in significant energy loss, which hinders practical application of the high-energy Li-O_2 battery. Oxyhalogen-sulfur electrochemistry offers a new hybrid Li-ion/Li-O_2 battery, where both Li ions and O anions are reversibly stored in the MoS_2 structure. A $Li_2MoO_2S_2$ compound is formed as the main discharge product that has never been previously observed in the literature. The reaction mechanism and the structure of the $Li_2MoO_2S_2$ are probed by Raman spectroscopy, X-ray photoelectron spectroscopy, X-ray absorption spectroscopy, differential electrochemical mass spectrometry, and UV-visible spectroscopy. The results show that the MoS_2 is oxidized during discharge and is recovered during charge. The iodine intermediates play an important role in triggering the sequence of electrochemical and chemical reactions in the cell. The $Li_2MoO_2S_2$ is isostructural to the Li_2MoO_4 rather than adopting structures of other known molybdenum oxysulfides.

Context & Scale

The lithium-oxygen (Li-O_2) battery is known for its high capacity but encounters large voltage hysteresis and poor cycling stability. In contrast, conventional Li-ion batteries have low polarization and long cycling life but show low capacity based on the intercalation chemistry. A combination of the Li-O_2 batteries and Li-ion batteries in one electrochemical system is expected to combine their advantages and avoid their disadvantages, which will show promise in meeting the future energy requirement. In this work, a hybrid Li-ion/Li-O_2 battery was constructed based on the oxyhalogen-sulfur electrochemistry. Both Li ions and O anions can be reversibly stored in the MoS_2 structure, forming a $Li_2MoO_2S_2$ compound. The iodine intermediates play an important role in triggering the sequence of electrochemical and chemical reactions in the cell. This hybrid Li-ion/Li-O_2 cell paves a way to push the limit of current Li-ion batteries and transition to the next generation of high-energy batteries.

INTRODUCTION

The discovery of a new material such as graphene[1] brought innovation to various research areas. For the energy-storage field, a potential high-energy system can be constructed based on a novel electrochemical reaction. Much effort has been made in both experimental and computational methods to find new compounds. One of the promising approaches is through the electrochemical process in chemical batteries where some thermodynamically metastable materials exist as intermediate products. The advantage of the electrochemical process is the ability to control the stoichiometric ratio precisely and continuously at room temperature. Electrochemical experiments have been useful in determining the phase diagram of well-known materials that include Li_xC_6 and Na_xCoO_2, which are known as intercalation battery materials.[2–4] More work needs to be done to discover new materials for high-energy-density batteries.

The aprotic Li-O_2 battery is a promising energy-storage technology because of its extremely high theoretical energy density (3,500 Wh kg^{-1} based on the reaction $2Li + O_2 \rightarrow Li_2O_2$).[5,6] However, for it to be a practical technology several challenges need to be addressed, for example, unclear reaction mechanism, large voltage hysteresis, unstable electrolyte, and Li-metal dendritic growth. Recent progress showed that the reaction pathway and discharge products vary depending on the electrolyte and catalyst species.[7] Electrolyte solvents with a high donor number promote the dissolution of LiO_2 intermediate to form Li_2O_2.[8,9] Disproportionating from unstable LiO_2 to Li_2O_2 can be partly inhibited by the iridium catalyst, forming LiO_2 as the main

Please cite this article in press as: Wang et al., Hybrid Li-Ion and Li-O_2 Battery Enabled by Oxyhalogen-Sulfur Electrochemistry, Joule (2018), https://doi.org/10.1016/j.joule.2018.07.019

discharge product.[10] Combining the reduced graphene oxide (rGO) and lithium iodide (LiI) results in LiOH formation; however, the electrochemical reversibility of the LiOH is still under debate.[11–14] Researchers aim to facilitate the sluggish reaction on the interface between the oxygen gas (O_2(g)), the Li ions in the liquid electrolyte, and the solid catalyst support. With the assistance of distinctive catalysts and/or redox mediators, the large voltage hysteresis of the Li-O_2 battery can be reduced to a certain extent, although it is still not comparable with that of Li-ion batteries based on the intercalation reaction.

The significant volume change of the cathode is another severe problem that hinders the practicality of Li-O_2 batteries. The accumulation of sporadic discharge products can clog the pores of the electrode. As a result, the battery shuts down. The host structure that leads the growth of solid discharge product and accommodates O_2(g) will keep the electrode active for long-term cycling.

Herein, a hybrid Li-ion/Li-O_2 battery based on two-dimensional molybdenum sulfide (MoS_2) is constructed to solve the aforementioned issues. MoS_2 is a well-known electrocatalysis in diverse fields of hydrodesulfurization (HDS),[15,16] photocatalysis,[17,18] hydrogen evolution reaction (HER),[19–21] and oxygen reduction reaction (ORR). Its large interlayer spacing with weak bond interaction allows foreign ions and molecules to intercalate.[22,23] With the assistance of LiI, both Li ions and O anions can be stored into the MoS_2 to form a compound, $Li_2MoO_2S_2$. The charge/discharge potential curves of this hybrid Li-ion/Li-O_2 battery almost overlap. The reaction mechanism is probed by Raman spectroscopy, X-ray photoelectron spectroscopy (XPS), X-ray absorption spectroscopy (XAS), differential electrochemical mass spectrometry (DEMS), and UV-visible spectroscopy. The enhanced kinetic reaction is due to the synergetic effect of the MoS_2, O_2, and LiI. Our findings provide a new insight and deeper understanding for the design of novel architecture for hybrid Li-ion/Li-O_2 batteries.

RESULTS

Edge-oriented MoS_2 nanosheets mounted on the rGO planes were designed as the cathode catalyst and to support the Li-O_2 batteries. Exposing the active MoS_2 edges enhances its catalytic performance.[24,25] Adding rGO forms a 3D electronic conductive network and guarantees fast charge transfer. Through the hydrothermal reaction (for the detailed method, see Supplemental Information), the rGO-MoS_2 composite grows on the stainless-steel mesh and its morphology is shown in Figure 1. As expected, MoS_2 nanosheets are vertically aligned on the rGO nanofilms. Electron-dispersive spectroscopy (EDS) mapping confirms the above architecture. The elemental carbon (Figure 1E) is evenly distributed while both elemental sulfur (S) (Figure 1F) and molybdenum (Mo) (Figure 1G) are confined in the local perpendicular sheets. Both the MoS_2 and rGO nanosheets are ultrathin (Figure 1B) and consist of a few atomic layers (Figure 1C). Such a few layered MoS_2 with open edges will greatly facilitate the reactions in Li-O_2 batteries, and its open structure may allow insertion of the oxygen anions.

The electrochemical performance of the rGO-MoS_2 is evaluated in a specially designed coin cell with pores on the cathode cap. The electrolyte contained 0.25 mol L^{-1} lithium bis(trifluoromethyl) sulfonylimide/dimethoxyethane (LiTFSI/DME) with 0.05 mol L^{-1} LiI additive. Adding LiI as a redox mediator facilitates the reactions in Li-O_2 batteries (Figures 2 and S1). Figure 2A shows the potential curves of rGO-MoS_2 when both the discharge and charge capacities are limited to

[1]Department of NanoEngineering, University of California San Diego, 9500 Gilman Drive, La Jolla, CA 92093, USA

[2]Chemical Sciences and Engineering Division, Argonne National Laboratory, Argonne, IL 60439, USA

[3]X-ray Science Division, Advanced Photon Sources, Argonne National Laboratory, Lemont, IL 60439, USA

[4]Materials Science and Engineering, University of California San Diego, 9500 Gilman Drive, La Jolla, CA 92093, USA

[5]Lead Contact

*Correspondence: junlu@anl.gov (J.L.), shirleymeng@ucsd.edu (Y.S.M.)

https://doi.org/10.1016/j.joule.2018.07.019

Please cite this article in press as: Wang et al., Hybrid Li-Ion and Li-O_2 Battery Enabled by Oxyhalogen-Sulfur Electrochemistry, Joule (2018), https://doi.org/10.1016/j.joule.2018.07.019

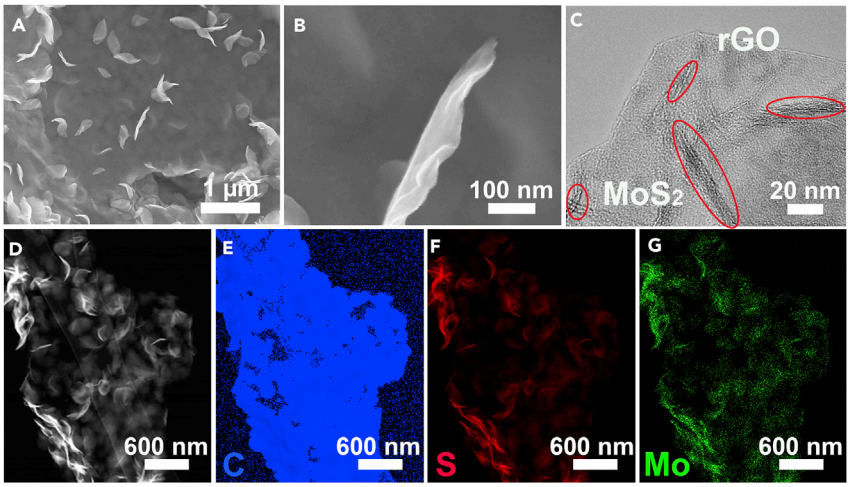

Figure 1. Morphology of the rGO-MoS_2 Composite

(A and B) Scanning electron microscopy images at different magnifications.

(C) Transmission electron microscopy image.

(D–G) Scanning transmission electron microscopy images and the corresponding EDS mappings. Blue, red, and green in (E), (F), and (G) stand for the elemental carbon (C), sulfur (S), and molybdenum (Mo), respectively.

500 mAh g^{-1} (calculated by the weight of the rGO-MoS_2). At the first discharge, the potential curve looks normal with a plateau around 2.65 V, and the charge process finishes before 3.0 V. However, at the second discharge it begins with a novel upper plateau around 2.93 V with 315 mAh g^{-1} capacity followed by a typical low plateau around 2.68 V with 150 mAh g^{-1} capacity. With continuing cycles, the low plateau gradually vanishes while the upper plateau becomes dominant. It is worth noting that the potential curves of the rGO-MoS_2 almost overlap at the 20th cycle (Figure 2A), similar to that of the conventional Li-ion batteries based on the intercalation chemistry. The voltage gap (the potential difference between the charge and discharge at 250 mAh g^{-1}) is as low as 20 mV and increases slightly after 50 cycles with an energy efficiency approaching 99%. This unique feature is very promising for making Li-O_2 batteries of practical use.

To find out the main contributors giving such distinctive potential curves of rGO-MoS_2, we conducted a series of controlled experiments at the same current density (50 mA g^{-1}) and capacity (500 mAh g^{-1}), the results of which are shown in Figures 2B, S1, and S2. It is obvious that a combination of MoS_2, LiI and O_2(g) is essential to achieve the above lowest polarization (Figures 2B and S1). Absence of any of them will lead to different potential curves and larger voltage hysteresis. Further adjusting the rGO-MoS_2 loading and LiI amount results in the similar potential curves (Figure S2), demonstrating that this kind of potential curve is more related to the nature of the MoS_2 rather than the LiI in the Li-O_2 battery. The distinctive potential curve of rGO-MoS_2 with LiI (Figures 2 and S1), especially the unique upper discharge plateau around 2.93 V, indicates alternative reaction mechanisms associated with MoS_2, Li ions and O_2(g).

To investigate the reaction mechanism of the rGO-MoS_2 with LiI, we utilized a series of characterization techniques. Figure 3 demonstrates the results obtained by scanning electron microscopy, Raman spectroscopy, XPS, and XAS. When the cell was first discharged to 300 mAh g^{-1}, no obvious morphology changes (Figure 3B)

Please cite this article in press as: Wang et al., Hybrid Li-Ion and Li-O_2 Battery Enabled by Oxyhalogen-Sulfur Electrochemistry, Joule (2018), https://doi.org/10.1016/j.joule.2018.07.019

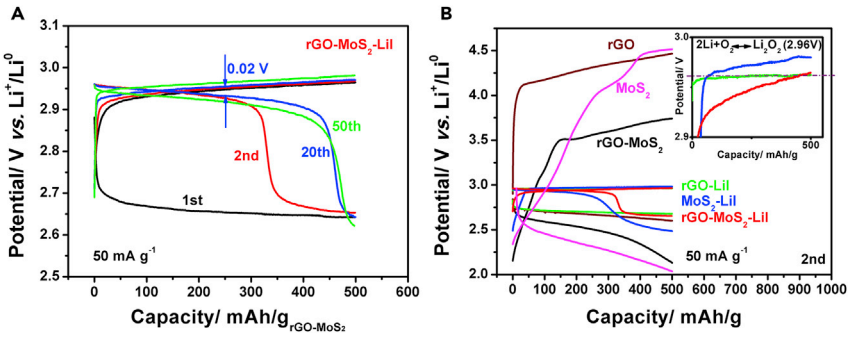

Figure 2. Potential Curves of Different Electrodes at 0.1 C

(A) Selected potential curves of the rGO-MoS_2 with LiI at different cycles.

(B) Compared potential curves of rGO, MoS_2, and rGO-MoS_2 with and without LiI at the second cycle.

were observed (see Figure 3A for the original morphology). Further discharging the cell to 500 mAh g^{-1} produces some porous flocculent sheets covering the rGO-MoS_2 (Figure 3C). These sheets are completely removed when the cell is charged to 500 mAh g^{-1} (Figure 3D). The morphology recovery after the first cycle indicates that reversible reactions occurred in the cell.

Raman spectroscopy results show that a set of new peaks appeared prominently at 503, 900, and 1,441 cm^{-1} at the discharge state (Figure 3E). These peaks are different from any characteristic Raman peaks pertaining to the rGO (D band centered at 1,347 cm^{-1} and G band centered at 1,585 cm^{-1}), MoS_2 (E^1_{2g} band centered at 375 cm^{-1} and A_{1g} band centered at 402 cm^{-1})[26] and other potential discharge products, such as Li_2O_2 (795 cm^{-1}), LiO_2 (1,123 and 1,505 cm^{-1}), LiOH (331 and 600 cm^{-1}), Li_2O (521 cm^{-1}), and Li_2CO_3 (1,093 cm^{-1}).[10,27,28] In fact, these new peaks can be ascribed to the vibration among Mo-O (900 cm^{-1})[29] and S-O (503 and 1,441 cm^{-1})[30] bonds, suggesting that the O anions are chemically adsorbed on the MoS_2 after discharge. The intense Mo-S and S-O Raman peaks suggest compound Li-Mo-O-S forms. These new bonds fade after charge (Figure 3E), which demonstrates the electrochemical reaction reversibility between O_2(g) and MoS_2.

XPS results demonstrate the oxidation and reduction of the MoS_2 during cycling (Figures 3F and 3G). After discharge, part of S and Mo are oxidized to a high valence to form sulfone (Figure 3F)[31] and Mo^{6+} (Figure 3G), respectively. After charge, they return to their original state. Since the signal detected by the XPS is from the surface, XAS was used to detect the chemical state change of the bulk of MoS_2. The results show that Mo is oxidized after discharge and can be further oxidized with multiple cycles, which is consistent with the XPS results. This is evidenced by the shift of the edge adsorption to the higher energy (Figure 3H), and the 2.93-V plateau dominates the potential curves after 20 cycles (Figure 2A). It is worth mentioning that the oxidation of MoS_2 mainly occurs within the first 300 mAh g^{-1} discharge capacity, as indicated by the negligible energy shift of the Mo adsorption edge (Figure 3H) and slight changes of the S 2p (Figure 3F) and Mo 3d (Figure 3G) spectra when the cell was further discharged from 300 mAh g^{-1} to 500 mAh g^{-1}. These results suggest that two different mechanisms take place consecutively. First, O_2(g) reacts with MoS_2 and Li ions to form a Li-Mo-S-O compound. Second, O_2(g) reacts with Li ions to form Li_2O_2, which is the dominant reaction product when the cell was further discharged to 2,000 mAh g^{-1} (Figure S3).

Please cite this article in press as: Wang et al., Hybrid Li-Ion and Li-O_2 Battery Enabled by Oxyhalogen-Sulfur Electrochemistry, Joule (2018), https://doi.org/10.1016/j.joule.2018.07.019

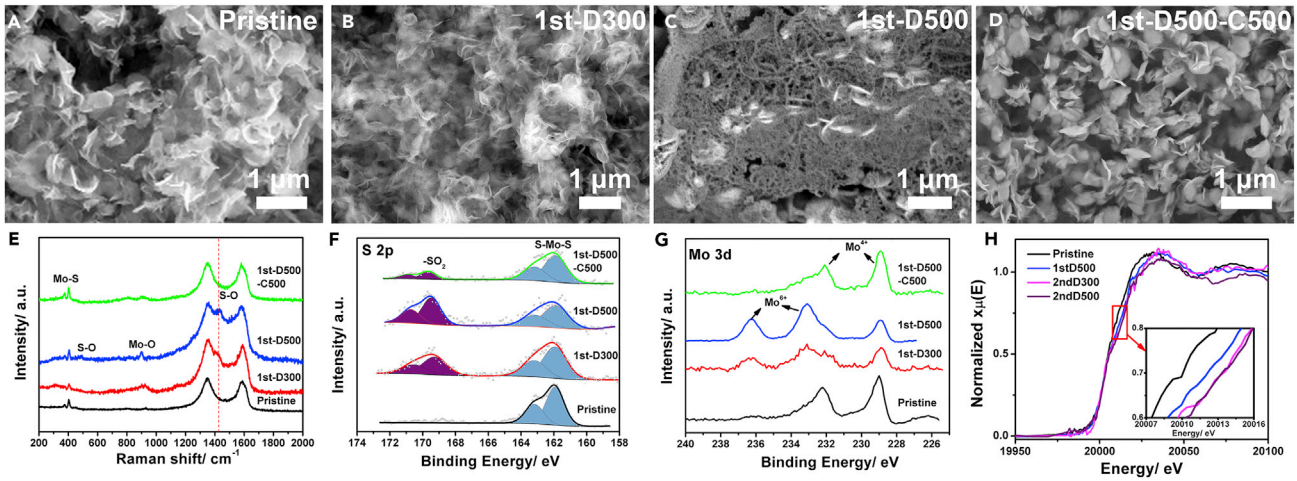

Figure 3. Characterization of the rGO-MoS_2 Electrode with LiI at Different Discharge/Charge States

(A–D) The corresponding scanning electron microscopy images of the rGO-MoS_2 electrode when the cell was firstly discharged to 0 mAh g^{-1} (denoted as pristine, A), 300 mAh g^{-1} (denoted as 1st-D300, B), 500 mAh g^{-1} (denoted as 1st-D500, C), and then charged to 500 mAh g^{-1} (denoted as 1st-D500-C500, D).

(E–G) Raman spectra (E), S 2p (F), and Mo 3d (G) XPS spectra of the pristine, 1st-D300, 1st-D500, and 1st-D500-C500 rGO-MoS_2 electrode.

(H) XAS spectra (H) from the pristine, 1st-D500, 2nd-D300, and 2nd-D500 rGO-MoS_2 electrode.

Based on the charge and ion transfer number associated with the first 300 mAh g^{-1} capacity (Figure 2A), the initial discharge product is believed to be $Li_2MoO_2S_2$. This is a new material that is not recorded in any of references and databases (e.g., Inorganic Crystal Structure Database). To determine the phase structure we carried out synchrotron X-ray diffraction (XRD), the results of which are shown in Figures 4A and S4. After discharge, a set of new peaks appears and the intensity is enhanced with multiple cycles. These peaks do not match any characteristic patterns of MoS_2, Li_2O_2, or LiOH; however, they are quite similar to that of Li_2MoO_4 (Figures 4A and S5). By substituting half of the O atoms in Li_2MoO_4 with S atoms, the XRD pattern can be well refined and the structure of the $Li_2MoO_2S_2$ is determined (Figure 4B and Table S1). As shown in Figure 4B, both Mo and Li atoms coordinate with the O and S atoms to form MoO_2S_2 and LiO_2S_2 tetrahedrons. These corner-linked tetrahedrons form a large hexagonal channel and a small distorted hexagonal channel along the crystallographic "*c*" axis. Compared with the pristine MoS_2 structure, incorporating the Li-O zigzag chain into the MoS_2 structure changes the previous MoS_6 triangular prisms to MoO_2S_2 tetrahedrons. The O chains bridge the interlayers connecting the structure together (Figure 4B).

The $Li_2MoO_2S_2$ is obtained in the Li-O_2 cell with MoS_2 and LiI through electrochemical reactions. The absence of MoS_2 and LiI leads to form LiOH and Li_2O_2 in the main reaction products (Figure S3). Considering the cofunction of MoS_2, LiI, and O_2(g) to form $Li_2MoO_2S_2$, it is likely to occur through oxyhalogen-sulfur electrochemical reactions. In the typical oxyhalogen-sulfur chemical reaction, the organic sulfur compounds react with iodates (e.g., HIO, HIO_2, and HIO_3) and are oxidized to form sulfoxides (Reaction 1).[32,33]

$$HIO + : \; SR_1R_2 \rightarrow R_1R_2S = O + H^+ + I^-. \qquad \text{(Reaction 1)}$$

In this case, under an electric field, the inorganic MoS_2 is oxidized by IO^- (Reaction 1) and inserted by Li ions to form $Li_2MoO_2S_2$ by a sequence of electrochemical and chemical reactions (Reaction 2). The total reaction is

Please cite this article in press as: Wang et al., Hybrid Li-Ion and Li-O_2 Battery Enabled by Oxyhalogen-Sulfur Electrochemistry, Joule (2018), https://doi.org/10.1016/j.joule.2018.07.019

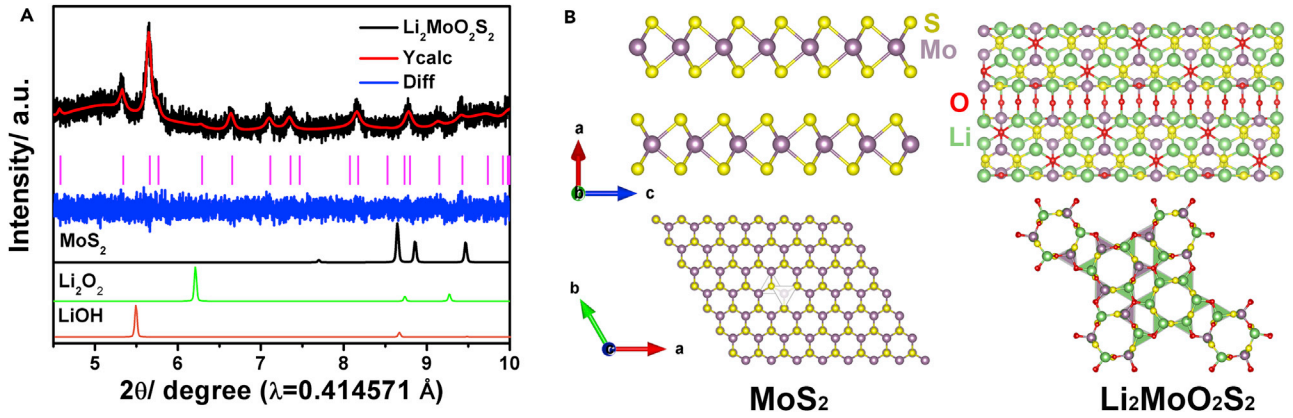

Figure 4. Structure of $Li_2MoO_2S_2$

(A and B) Refined synchrotron XRD pattern of the $Li_2MoO_2S_2$ at seventh discharge (A) and comparison of structural schematic between MoS_2 and $Li_2MoO_2S_2$ (B).

$$O_2 + MoS_2 + 2Li^+ + 2e^- \overset{LiI}{\leftrightarrow} Li_2MoO_2S_2. \qquad \text{(Reaction 2)}$$

Based on Reaction 2, the theoretical capacity is calculated to be 335 mAh $g^{-1}_{(MoS2)}$, which is consistent with the capacity at the upper plateau around 2.93 V (Figure 2A). According to Reaction 1, IO^- is the key to trigger the oxyhalogen-sulfur electrochemical reaction. In the Li-O_2 battery, IO^- is formed by the reaction between superoxide, LiI, and trace water in electrolyte,[34] which was captured in the electrolyte by UV-visible spectroscopy (Figures 5A and S6A) and Raman spectroscopy (Figures 5B and S6B). The adsorption peak at 284 nm (Figure 5A) and vibration peaks at 486 and 554 cm^{-1} (Figure 5B) belong to IO^- radical,[35–38] which appears at the discharge state and vanishes at the charge state.

To track the reversibly O_2(g) consumption and evolution involved in the cycling, we performed DEMS with tetraethylene glycol DME. DME was replaced due to its high volatility. These two solvents showed identical electrochemical behavior (Figure S7). As shown in Figure 5C, during discharge the O_2(g) is continually consumed at a rate of $1e^-/O_2$ at the beginning, indicating the formation of superoxide and its stabilization by iodide. At the end of the discharge, the rate is close to $2e^-/O_2$, which is consistent with the formation of $Li_2MoO_2S_2$ and Li_2O_2. The total molar ratio of e^-/O_2 is about 1.7, less than 2, indicating that some O anion is trapped in the electrolyte in the forms of O_2^-/IO^-. O_2(g) is released in the following charge and no other gas (CO_2 and H_2) is detected (Figure 5D), demonstrating the high reversibility of the ORR/oxygen evolution reaction (OER) processes and negligible side reactions. Similar ORR/OER behavior was found in the second cycle (Figure S8) although their discharge potential curves were different. The low potential at the first discharge is due to the formation of the O_2^-/IO^- radicals while some of these radicals remain in the electrolyte after first discharge (3.6 μmol O_2 evolution versus 3.9 μmol O_2 consumption at the first cycle; Figures 5C and 5D). Therefore, the first cycling can be regarded as an activation process. Thereafter, the characteristic potential curve of MoS_2 shows up from the second cycle via Reaction 2, which corresponds to the upper discharge plateau around 2.93 V (Figure 2A).

The reaction mechanism of rGO-MoS_2 cell with LiI is summarized in Figure 6. At the discharge, the O_2(g) is firstly reduced to O_2^-. The O_2^- reacts with the LiI and trace amount of H_2O in the electrolyte to form IO^-, then the IO^- oxidizes the MoS_2. Subsequently, Li ions instantly insert into the structure to form $Li_2MoO_2S_2$. The resultant

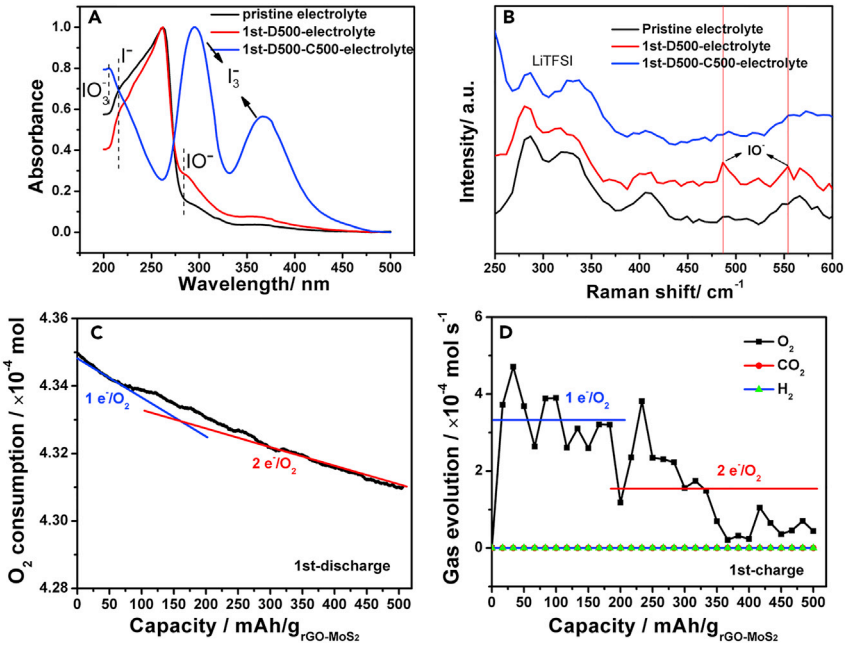

Q15 Figure 5.

(A–D) UV spectra (A) and Raman spectra (B) of the pristine, post first discharge, and charge electrolytes; DEMS spectra during first discharge (C) and charge (D) states.

base electrolyte is favorable in generating Li_2O_2 rather than LiOH.[39] Therefore, $Li_2MoO_2S_2$ is the synergetic result of O_2(g), MoS_2, LiI, and trace amount of H_2O via the oxyhalogen-sulfur electrochemical reactions. Both LiI and H_2O are essential mediators, and increasing each concentration is beneficial to facilitating the reaction (Figure S9). In contrast, the nanostructure of rGO-MoS_2 is not necessary since the commercial microsize MoS_2 also has similar behavior (Figure S10). Obviously, the nanoarchitecture design of MoS_2 with rGO contributes to enhancement of the kinetic reaction (Figure S11A) and cycling stability (Figure S11B) by providing high surface-active sites and a good conductive network. After more than 100 cycles, the main discharge product is $Li_{2x}MoO_{2x}S_2$ ($x > 1$) (Figure S12) and the charge compensation is provided by MoS_2 (Figure S13).

At the following charge, the I^- is first oxidized to I_3^- by electrochemical process, whose presence is evidenced by the UV spectra (Figure 5A). Besides I_3^-, IO_3^- also exists in the electrolyte, which shows a characteristic peak at ~207 nm in the UV spectra of electrolyte (Figure 5A).[40] A mixture of I^-, I_3^-, IO^-, and trace H_2O in the electrolyte could disproportionate into different species of the iodine intermediates, such as IO_3^-.[41,42] Their disproportionation pathway and rate will be affected by the electrochemical reactions inside the cell. These I-intermediates are believed to promote the decomposition of Li_2O_2 and $Li_2MoO_2S_2$ to release the O_2(g) by chemical reactions (Figure 6).[34,43] The chemical reaction between $Li_2MoO_2S_2$, I_3^-, and trace H_2O is confirmed since the Mo-O bond gradually vanishes when the $Li_2MoO_2S_2$ is immersed in the I_3^- /DME solution with 500 ppm H_2O (Figure S14). In addition, part of the Li_2O_2 and $Li_2MoO_2S_2$ are supposed to decompose by electrochemical reactions. For clarification of the charge mechanism, more experimental and computational work is needed to understand the physical/(electro)chemical properties of the $Li_2MoO_2S_2$. For example, the chemical stability of the $Li_2MoO_2S_2$ at the charge/discharge state needs to be evaluated since some thiomolybdates are found

Please cite this article in press as: Wang et al., Hybrid Li-Ion and Li-O_2 Battery Enabled by Oxyhalogen-Sulfur Electrochemistry, Joule (2018), https://doi.org/10.1016/j.joule.2018.07.019

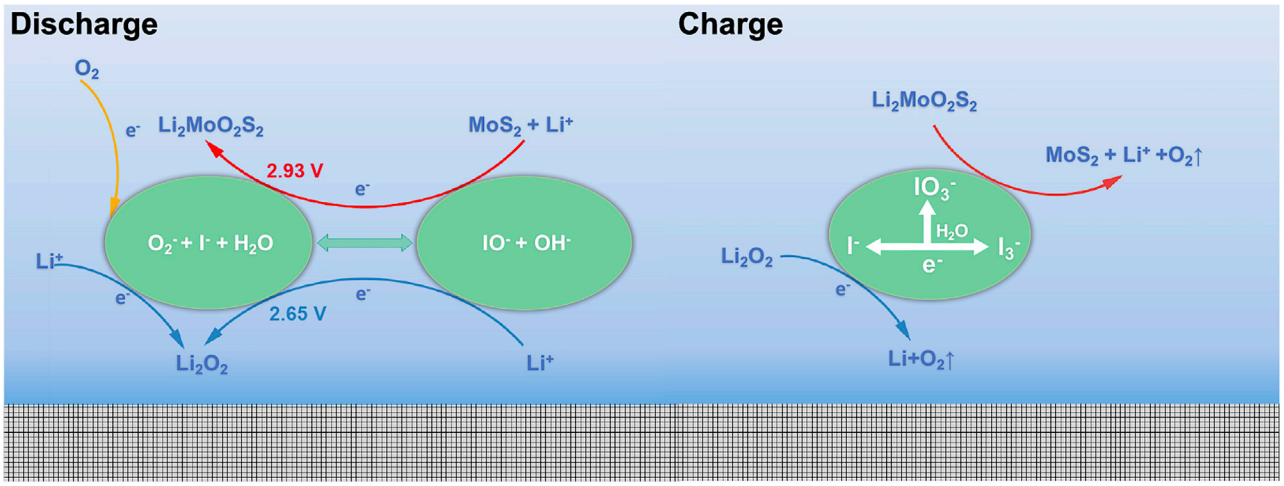

Figure 6. Schematic of Reaction Mechanism of rGO-MoS_2 with LiI during Discharge and Charge

to be sensitive to the solution properties, such as pH, and will convert to other intermediate thiomolybdates (MoO_3S^{2-}, $MoO_2S_2^{2-}$, and $MoOS_3^{2-}$).[44–46]

DISCUSSION

As demonstrated herein, the rGO-MoS_2 cell requires Li, MoS_2, O_2(g), and LiI for the electrochemical reactions, which combine the characteristic cell configuration (host and O_2) and electrochemical performance (low polarization and high capacity) of the conventional Li-ion battery and Li-O_2 battery. In other words, this is a hybrid Li-ion/Li-O_2 cell. The concept of the hybrid Li-ion/Li-O_2 cell was first proposed by Thackeray et al., who used the high Li_2O-containing metal oxides, such as Li_5FeO_4, to release the Li and O_2(g) during charge and produced Li_2O-metal oxide compounds during discharge.[47–49] In this case, a Li_2O_2-MoS_2 compound, $Li_2MoO_2S_2$, is formed during discharge. It releases the Li and O_2(g) during charge. When the discharge capacity is beyond the storage capability of MoS_2, Li_2O_2 will form as discharge products (Figure S3) and the cell will behave like a conventional Li-O_2 battery.

Considering the low polarization and high capacity, the rGO-MoS_2-O_2 cell demonstrates a very promising prototype for constructing a useful hybrid Li-ion/Li-O_2 battery. The key is to find a suitable host, for example MoS_2, which should meet the following criteria. (1) MoS_2 provides enough room to store the Li ions and O anions, forming the $Li_2MoO_2S_2$ compound. After activation, the maximum capacity of the hybrid rGO-MoS_2-O_2 cell is about 1,000 mAh $g^{-1}_{(MoS2)}$ (Figure S15). (2) The oxidized MoS_2 has compatible working voltage window with Li_2O_2.[50] In contrast, the voltage hysteresis of Li_5FeO_4 is as large as 2.0 V.[47] The large voltage mismatch will lead to much energy loss of the cell. (3) The structure of MoS_2 is robust for long-term use. It recovers after charge and remains stable for hundreds of cycles (Figure S11).

To facilitate the kinetic reactions, catalysts or redox mediators also work well in the hybrid Li-ion/Li-O_2 battery, such as LiI. LiI plays a vital role in the hybrid rGO-MoS_2-O_2 cell. (1) LiI combines with O_2^- to form IO^-, promotes the dissolution of the O_2^- into the electrolyte, and alters the reaction through solution. (2) IO^- triggers oxidization of the MoS_2 and forms the $Li_2MoO_2S_2$ by oxyhalogen-sulfur electrochemistry. (3) Other iodine intermediates promote decomposition of $Li_2MoO_2S_2$, which lowers the cell overpotential. (4) LiI also catalyzes the formation and decomposition of Li_2O_2.[43]

Compared with the conventional Li-O_2 battery, the hybrid Li-ion/Li-O_2 cell outperforms in several aspects: (1) low polarization; (2) the O anions are accommodated in the structure of the MoS_2, which restricts the volume changes and eliminates the common clogging problem caused by unevenly accumulated Li_2O_2;[51] (3) the low charge voltage reduces the harmful coverage by side-products. In short, the hybrid Li-ion/Li-O_2 cell combines the advantages of Li-ion and Li-O_2 batteries, and shows promise in meeting future energy requirements.

The compound $Li_2MoO_2S_2$ is found to be isostructural to the Li_2MoO_4 (Figure S5) rather than the other molybdenum oxysulfides $A_2MoO_2S_2$ (A = K, Rb, Cs, and NH_4).[52,53] This is mostly due to the similar ionic size of the Li^+ (60 pm) and the Mo^{6+} (62 pm) while other cations are very large (K^+ [133 pm], Rb^+ [148 pm], Cs^+ [169 pm], and $(NH)_4^+$ [148 pm]). Therefore, both Mo and Li atoms can coordinate with the two O and two S atoms to form MoO_2S_2 and LiO_2S_2 tetrahedrons while other large cations require more anion atoms to form complex polyhedrons. This unique structure is expected to endow $Li_2MoO_2S_2$ with some interesting physical/chemical properties. The $Li_2MoO_2S_2$ can be obtained through both the electrochemical (in this case) and chemical reactions (Figure S16).

Since various species such as O_2(g), MoS_2(solid [s]), rGO(s), LiI(liquid [l]), H_2O(l), and electrolyte(l) are integrated in one electrochemical system, a series of electrochemical and chemical reactions could occur besides the dominant reactions proposed above.[34] It is difficult to segregate each contribution because some of them are synergetic and require more characterizations and control experiments, which are beyond the scope of this paper. DME was used because it is more stable than other solvents, such as DMSO.[54] However, electrolyte decomposition was still found (Figure S12) and accumulation of the by-products such as Li_2CO_3 will passivate the catalyst, block the reaction, and increase the polarization. Therefore, it is still challenging to clarify the complex mechanism and have a stable electrolyte for practical Li-O_2 battery.

In summary, based on the oxyhalogen-sulfur electrochemistry, a hybrid Li-ion/Li-O_2 battery was constructed, which combines the features of the Li-O_2 batteries and Li-ion batteries. Both Li ions and O anions can be reversibly stored in the MoS_2 structure, forming a $Li_2MoO_2S_2$ compound. The reaction mechanism was explained by using Raman spectroscopy, DEMS, XPS, XAS, and XRD. It was found that the dissolved O_2^- combines with I^- to oxidize MoS_2, which allows Li^+ intercalation into the MoS_2 structure. The integrated MoS_2 is oxidized upon the discharge state and recovered upon the charge state.

We have attempted chemical synthesis to isolate $Li_2MoO_2S_2$ without any success, as it is the first time the compound has been observed in an electrochemical system. More fundamental study is needed to explore its physical/(electro)chemical properties.

EXPERIMENTAL PROCEDURES

Full experimental procedures are provided in the Supplemental Information.

SUPPLEMENTAL INFORMATION

Supplemental Information includes Supplemental Experimental Procedures, 16 figures, and 1 table and can be found with this article online at https://doi.org/10.1016/j.joule.2018.07.019.

ACKNOWLEDGMENTS

We acknowledge the use of the University of California, San Diego Cryo-Electron Microscopy Facility, which is supported by NIH grants to Dr. Timothy S. Baker and a gift from the Agouron Institute to UCSD. The scanning EM was performed in part at the San Diego Nanotechnology Infrastructure (SDNI), a member of the National Nanotechnology Coordinated Infrastructure, which is supported by the National Science Foundation (grant ECCS-1542148). XPS work was performed at the University of California, Irvine Materials Research Institute using instrumentation funded in part by the National Science Foundation Major Research Instrumentation Program under grant no. CHE-1338173. We thank the Advanced Photon Source for the synchrotron X-ray diffractions (beamline 11-BM) and XAS (beamline 20-BM) at the Argonne National Laboratory. X.W. appreciates the discussion and help from Dr. Yurui Gao and Dr. Longfei Wang. M.S. acknowledges Qualcomm Company for the use of scanning transmission electron microscopy facilities. We are grateful for financial support from the Assistant Secretary for Energy Efficiency and Renewable Energy, Office of Vehicle Technologies of the US Department of Energy under the Battery500 Consortium. Partial funding is provided by Assistant Secretary for Energy Efficiency and Renewable Energy, Office of Vehicle Technologies of the US Department of Energy under contract no. DE-AC02-05CH11231, subcontract no. 7073923, under the Advanced Battery Materials Research Program.

AUTHOR CONTRIBUTIONS

X.W. conceived the idea, designed the experiments, and conducted most of the characterizations. Y.L. and B.L. helped to synthesize the materials. Y.L. performed the density functional theory calculations. X.B. and J.L. carried out the DEMS. L.M. and T.W. performed the XAS. M.S. conducted the scanning transmission electron microscopy. S.W. helped with UV. X.W., J.L., and Y.S.M. analyzed the experimental and computational data together. All authors (the aforementioned and M.Z., J.A., A.B., and K.A.) discussed the results and commented on the manuscript. The manuscript was written through contributions of all authors. All authors have given approval of the final version of the manuscript.

DECLARATION OF INTERESTS

X.W. and Y.S.M. are the inventors on a US provisional invention disclosure related to this work.

Received: February 17, 2018
Revised: May 30, 2018
Accepted: July 19, 2018
Published: August 9, 2018

REFERENCES

1. Novoselov, K.S. (2004). Electric field effect in atomically thin carbon films. Science *306*, 666–669.

2. Filhol, J.S., Combelles, C., Yazami, R., and Doublet, M.L. (2008). Phase diagrams for systems with low free energy variation: a coupled theory/experiments method applied to Li-graphite. J. Phys. Chem. C *112*, 3982–3988.

3. Berthelot, R., Carlier, D., and Delmas, C. (2011). Electrochemical investigation of the P_2-$NaxCoO_2$ phase diagram. Nat. Mater. *10*, 74–80.

4. Lu, J.C., Chung, S.C., Nishimura, S., and Yamada, A. (2013). Phase diagram of olivine Na_xFePO_4 ($0 < x < 1$). Chem. Mater. *25*, 4557–4565.

5. Zhang, J., Ma, Z., Yuan, X., Li, L., Ma, Z.-F., Wilkinson, D.P., and Zhang, L. (2015). A review of cathode materials and structures for rechargeable lithium-air batteries. Energy Environ. Sci. *8*, 2144–2198.

6. Feng, N., He, P., and Zhou, H. (2016). Critical challenges in rechargeable aprotic Li-O_2 batteries. Adv. Energy Mater. *6*, 1502303.

7. Aurbach, D., McCloskey, B.D., Nazar, L.F., and Bruce, P.G. (2016). Advances in understanding mechanisms underpinning lithium–air batteries. Nat. Energy *1*, 16128.

8. Johnson, L., Li, C., Liu, Z., Chen, Y., Freunberger, S.A., Ashok, P.C., Praveen, B.B., Dholakia, K., Tarascon, J.M., Bruce, P.G., et al. (2014). The role of LiO_2 solubility in O_2 reduction in aprotic solvents and its

consequences for Li-O_2 batteries. Nat. Chem. *6*, 1091–1099.

9. Gao, X., Chen, Y., Johnson, L., and Bruce, P.G. (2016). Promoting solution phase discharge in Li-O_2 batteries containing weakly solvating electrolyte solutions. Nat. Mater. *15*, 882–888.

10. Lu, J., Lee, Y.J., Luo, X., Lau, K.C., Asadi, M., Wang, H.H., Brombosz, S., Wen, J., Zhai, D., Chen, Z., et al. (2016). A lithium-oxygen battery based on lithium superoxide. Nature *529*, 377–382.

Q11

11. Liu, T., Leskes, M., Yu, W., Moore, A.J., Zhou, L., Bayley, P.M., Kim, G., and Grey, C.P. (2015). Cycling Li-O_2 batteries via LiOH formation and decomposition. Science *350*, 530–533.

12. Burke, C.M., Black, R., Kochetkov, I.R., Giordani, V., Addison, D., Nazar, L.F., and McCloskey, B.D. (2016). Implications of 4 e^- oxygen reduction via iodide redox mediation in Li-O_2 batteries. ACS Energy Lett. 747–756.

13. Shen, Y., Zhang, W., Chou, S.-L., and Dou, S.-X. (2016). Comment on "cycling Li-O_2 batteries via LiOH formation and decomposition". Science *352*, 667.

14. Viswanathan, V., Pande, V., Abraham, K.M., Luntz, A.C., McCloskey, B.D., and Addison, D. (2016). Comment on "cycling Li-O_2 batteries via LiOH formation and decomposition". Science *352*, 667.

15. Muller, A. (1986). Coordination chemistry of Mo-and WS compounds and some aspects of hydrodesulfurization catalysis. Polyhedron *5*, 323–340.

16. Byskov, L.S., Nørskov, J.K., Clausen, B.S., and Topsøe, H. (1999). DFT calculations of unpromoted and promoted MoS_2-based hydrodesulfurization catalysts. J. Catal. *187*, 109–122.

Q12

17. Li, Y., Li, Y.-L., Araujo, C.M., Luo, W., and Ahuja, R. (2013). Single-layer MoS_2 as an efficient photocatalyst. Catal. Sci. Technol. *3*, 2214–2220.

18. Parzinger, E., Miller, B., Blaschke, B., Garrido, J.A., Ager, J.W., Holleitner, A., and Wurstbauer, U. (2015). Photocatalytic stability of single- and few-layer MoS_2. ACS Nano *9*, 11302–11309.

19. Wang, H., Lu, Z., Xu, S., Kong, D., Cha, J.J., Zheng, G., Hsu, P.C., Yan, K., Bradshaw, D., Prinz, F.B., Cui, Y., et al. (2013). Electrochemical tuning of vertically aligned MoS_2 nanofilms and its application in improving hydrogen evolution reaction. Proc. Natl. Acad. Sci. USA *110*, 19701–19706.

20. Zhang, L., Wu, H.B., Yan, Y., Wang, X., and Lou, X.W. (2014). Hierarchical MoS_2 microboxes constructed by nanosheets with enhanced electrochemical properties for lithium storage and water splitting. Energy Environ. Sci. *7*, 3302–3306.

21. Li, H., Du, M., Mleczko, M.J., Koh, A.L., Nishi, Y., Pop, E., Bard, A.J., and Zheng, X. (2016). Kinetic Study of hydrogen evolution reaction over strained MoS_2 with sulfur vacancies using scanning electrochemical microscopy. J. Am. Chem. Soc. *138*, 5123–5129.

22. Benavente, E., Santa Ana, M.A., Mendizábal, F., and González, G. (2002). Intercalation chemistry of molybdenum disulfide. Coord. Chem. Rev. *224*, 87–109.

23. Huang, X., Zeng, Z., and Zhang, H. (2013). Metal dichalcogenide nanosheets: preparation, properties and applications. Chem. Soc. Rev. *42*, 1934–1946.

24. Jaramillo, T.F., Jorgensen, K.P., Bonde, J., Nielsen, J.H., Horch, S., and Chorkendorff, I. (2007). Identification of active edge sites for electrochemical H_2 evolution from MoS_2 nanocatalysts. Science *317*, 100–102.

25. Kibsgaard, J., Chen, Z., Reinecke, B.N., and Jaramillo, T.F. (2012). Engineering the surface structure of MoS_2 to preferentially expose active edge sites for electrocatalysis. Nat. Mater. *11*, 963–969.

26. Wieting, T.J., and Verble, J.L. (1971). Infrared and Raman studies of long-wavelength optical phonons in hexagonal MoS_2. Phys. Rev. B *3*, 4286–4292.

27. Gittleson, F.S., Ryu, W.-H., and Taylor, A.D. (2014). Operando observation of the gold–electrolyte interface in Li-O_2 batteries. ACS Appl. Mater. Interfaces *6*, 19017–19025.

28. Gittleson, F.S., Yao, K.P.C., Kwabi, D.G., Sayed, S.Y., Ryu, W.-H., Shao-Horn, Y., and Taylor, A.D. (2015). Raman spectroscopy in lithium-oxygen battery systems. Chemelectrochem. *2*, 1446–1457.

29. Barinova, O., Kirsanova, S., Sadovskiy, A., and Avetissov, I. (2014). Properties of Li_2MoO_4 single crystals grown by Czochralski technique. J. Cryst. Growth *401*, 853–856.

30. Lin-Vien, D., Colthup, N.B., Fateley, W.G., and Grasselli, J.G. (1991). Organic sulfur compounds. In The Handbook of Infrared and Raman Characteristic Frequencies of Organic Molecules (Academic Press), pp. 225–250.

31. Lindberg, B.J., Hamrin, K., Johansson, G., Gelius, U., Fahlman, A., Nordling, C., and Siegbahn, K. (1970). Molecular spectroscopy by means of ESCA II. Sulfur compounds. Correlation of electron binding energy with structure. Phys. Scr. *1*, 286.

32. Mundoma, C., and Simoyi, R.H. (1997). Oxyhalogen-sulfur chemistry Oxidation of 2-aminoethanethiolsulfuric acid by iodate in acidic medium. J. Chem. Soc. Faraday Trans. *93*, 1543–1550.

33. Chikwana, E., Davis, B., Morakinyo, M.K., and Simoyi, R.H. (2009). Oxyhalogen-sulfur chemistry—kinetics and mechanism of oxidation of methionine by aqueous iodine and acidified iodate. Can. J. Chem. *87*, 689–697.

34. Qiao, Y., Wu, S., Sun, Y., Guo, S., Yi, J., He, P., and Zhou, H. (2017). Unraveling the complex role of iodide additives in Li-O_2 batteries. ACS Energy Lett. 1869–1878.

35. Durig, J.R., Bonner, O.D., and Breazeale, W.H. (1965). Raman studies of iodic acid and sodium iodate. J. Phys. Chem. *69*, 3886–3892.

36. Haimovich, O., and Treinin, A. (1965). Electronic spectrum of IO^- in solution. Nature *207*, 185–186.

37. Paquette, J., and Ford, B.L. (1985). Iodine chemistry in the +1 oxidation state. I. The electronic spectra of OI^-, HOI, and H_2OI^+. Can. J. Chem. *63*, 2444–2448.

38. Wren, J.C., Paquette, J., Sunder, S., and Ford, B.L. (1986). Iodine chemistry in the +1 oxidation state. II. A Raman and UV-visible spectroscopic study of the disproportionation of hypoiodite in basic solutions. Can. J. Chem. *64*, 2284–2296.

39. Matsui, M., Wada, A., Matsuda, Y., Yamamoto, O., Takeda, Y., and Imanishi, N. (2015). A novel aqueous lithium-oxygen cell based on the oxygen-peroxide redox couple. Chem. Commun. *51*, 3189–3192.

40. Liu, T., Kim, G., Carretero-González, J., Castillo-Martínez, E., and Grey, C.P. (2016). Response to comment on "cycling Li-O_2 batteries via LiOH formation and decomposition". Science *352*, 667.

41. Furrow, S. (1987). Reactions of iodine intermediates in iodate-hydrogen peroxide oscillators. J. Phys. Chem. *91*, 2129–2135.

42. Liebhafsky, H.A., and Wu, L.S. (1974). Reactions involving hydrogen peroxide, iodine, and iodate ion. V. Introduction to the oscillatory decomposition of hydrogen peroxide. J. Am. Chem. Soc. *96*, 7180–7187.

43. Nakanishi, A., Thomas, M.L., Kwon, H.-M., Kobayashi, Y., Tatara, R., Ueno, K., Dokko, K., and Watanabe, M. (2018). Electrolyte composition in Li/O_2 batteries with LiI redox mediators: solvation effects on redox potentials and implications for redox shuttling. J. Phys. Chem. C *122*, 1522–1534.

44. Erickson, B.E., and Helz, G.R. (2000). Molybdenum(VI) speciation in sulfidic waters:: stability and lability of thiomolybdates. Geochim. Cosmochim. Acta *64*, 1149–1158.

45. Harmer, M.A., and Sykes, A.G. (1980). Kinetics of the interconversion of sulfido- and oxomolybdate(VI) species $MoO_xS_{4-x}^{2-}$ in aqueous solutions. Inorg. Chem. *19*, 2881–2885.

46. Prasad, T.P., Diemann, E., and Müller, A. (1973). Thermal decomposition of $(NH_4)_2MoO_2S_2$, $(NH_4)_2MoS_4$, $(NH_4)_2WO_2S_2$ and $(NH_4)_2WS_4$. J. Inorg. Nucl. Chem. *35*, 1895–1904.

47. Trahey, L., Johnson, C.S., Vaughey, J.T., Kang, S.-H., Hardwick, L.J., Freunberger, S.A., Bruce, P.G., and Thackeray, M.M. (2011). Activated lithium-metal-oxides as catalytic electrodes for Li-O_2 cells. Electrochem. Solid State Lett. *14*, A64–A66.

48. Thackeray, M.M., Chan, M.K.Y., Trahey, L., Kirklin, S., and Wolverton, C. (2013). Vision for designing high-energy, hybrid Li ion/Li-O_2 cells. J. Phys. Chem. Lett. *4*, 3607–3611.

49. Park, K.H., Bai, Q., Kim, D.H., Oh, D.Y., Zhu, Y., Mo, Y. and Jung, Y.S.. Design strategies, practical considerations, and new solution processes of sulfide solid electrolytes for all-solid-state batteries. Adv. Energy Mater. https://doi.org/10.1002/aenm.201800035.

50. Abraham, K.M., Pasquariello, D.M., and Willstaedt, E.B. (1989). Lithium/molybdenum oxysulfide secondary batteries. J. Electrochem. Soc. *136*, 576–577.

51. Lim, H.-D., Park, K.Y., Song, H., Jang, E.Y., Gwon, H., Kim, J., Kim, Y.H., Lima, M.D., Ovalle

Robles, R., and Lepró, X. (2012). Enhanced power and rechargeability of a Li-O_2 battery based on a hierarchical-fibril CNT electrode. Adv. Mater. *25*, 1348–1352.

52. Müller, A., Diemann, E., and Baran, E.J. (1970). Übergangsmetallchalkogenverbindungen. über dithiomolybdate und -wolframate $(NH_4)_2MoO_2S_2$ und $(NH_4)_2WO_2S_2$, Verbindungen mit starken Wasserstoffbrücken. Z. Anorg. Allg. Chem. *375*, 87–97.

53. Tsigdinos, G.A. (1978). Inorganic sulfur compounds of molybdenum and tungsten. In Topics in Current Chemistry: Aspects of Molybdenum and Related Chemistry, G.A. Tsigdinos and G.H. Moh, eds. (Springer), pp. 65–105.

54. Khetan, A., Luntz, A., and Viswanathan, V. (2015). Trade-offs in capacity and rechargeability in nonaqueous Li-O_2 batteries: solution-driven growth versus nucleophilic stability. J. Phys. Chem. Lett. *6*, 1254–1259.

JOUL, Volume *2*

Supplemental Information

Hybrid Li-Ion and Li-O_2 Battery Enabled by Oxyhalogen-Sulfur Electrochemistry

Xuefeng Wang, Yejing Li, Xuanxuan Bi, Lu Ma, Tianpin Wu, Mahsa Sina, Shen Wang, Minghao Zhang, Judith Alvarado, Bingyu Lu, Abhik Banerjee, Khalil Amine, Jun Lu, and Ying Shirley Meng

Supplementary information

Materials and methods:

Materials: All the chemicals were bought from Sigma Aldrich. The anhydrous 1,2-Dimethoxyethane (DME, for HPLC, 99.9%, inhibitor-free), lithium bis(trifluoromethyl) sulfonylimide (LiTFSI), lithium iodide (LiI) and dimethyl carbonate (DMC) were stored in the Ar filled glovebox (O_2<0.1 ppm, and H_2O<0.1 ppm). DME was further dried by the molecular sieves.

Synthesis of reduced graphene oxide (rGO): The rGO was prepared by a modified Hummer's method. The graphite (2 g) was oxidized by the concentrated H_2SO_4 (80 mL), HNO_3 (60 mL) and $KMnO_4$ (12 g). The mixture solution was continuously stirred at 0 ℃ for 1 hour and then at room temperature for another 24 h after adding 200 mL H_2O. 10 mL H_2O_2 (30%) was introduced into the solution and the color of the suspension was changed from brown to yellow. The graphene oxides (GO) were repeatedly washed with H_2O by centrifuging, then dispersed in H_2O by ultrasonicating and finally freeze-dried for 3 days. The rGO electrode was made by casting the GO slurry onto a stainless-steel mesh (SSM, Alfa, 325 mesh woven from 0.036 mm dimeter wire), freeze-drying and reducing at 550 ℃ for 2 hours in the Ar flowing tube furnace.

Synthesis of rGO-MoS_2: The free-standing rGO-MoS_2 electrode was obtained by directly growing the rGO-MoS_2 sheets on the SSM via hydrothermal reaction. The mixture solution of GO (5 mg), MoO_3 (30 mg), triacetamide (35 mg), urea (300 mg), ethanol (50 mL) and H_2O (30 mL) and SSM were putted into a 100 mL autoclave and hydrothermally treated at 200 ℃ for 24 hours. The yielded rGO-MoS_2 on SSM was washed and freeze-dried. Pure MoS_2 electrode was obtained as the same procedure but without rGO additive. The average loading of the active material on an electrode (diameter 13 mm) is about 0.2 mg.

Preparation of the commercial MoS_2 electrode: Commercial MoS_2, Super P carbon and polyvinylidene fluoride (PVDF) were mixed together at a weight ratio of 8:1:1 with N-Methyl-2-pyrrolidone (NMP) solvent and casted on the SSM. The loading of the MoS_2 is about 1.6 mg.

Cell assembly and electrochemical evaluation: Coin cells (R2032 for air batteries, MTI corporation) were assembled with a disc of lithium foil (1mm thickness, FMC), 500 μL electrolyte, two pieces of glass fiber separator (Whatman, grade GF/D), O_2 electrode and Ni foam (act as O_2 diffusion layer and electrons-transfer layer, MTI corporation). The electrolytes were 0.25 mol/L LiTFSI/DME with/without 50 mmol/L LiI. The

assembled coin cells were placed in the O_2 filled container and electrochemically tested at galvanostatic mode for the same discharge/charge time by LanHe battery cycler (Wuhan, China). All potentials are referenced against Li/Li^+. The electrochemical performance was reproduced for at least twice, especially for rGO-MoS_2 with LiI.

Electrode Characterization:

All the cycled samples were taken out from the batteries, rinsed with DMC, stored in the glovebox and tested in the dry atmosphere.

The TEM samples were loaded on lacy carbon grid and performed at a FEI-Tecnai Osiris microscope (200 kV) equipped with Super-X EDS detection system.

Synchrotron X-ray diffractions were taken at the Advanced Photon Source (APS) at Argonne National Laboratory (ANL) on beamline 11-BM (λ= 0.4145 Å). The beamline uses a sagittal focused X-ray beam with a high precision diffractometer circle and perfect Si (111) crystal analyzer detection for high sensitivity and resolution. XRD patterns were analyzed by the Rietveld refinement method using TOPAS software.

XPS was performed using a Kratos Ultra DLD XPS. All spectra were calibrated with C 1s (284.8 eV) of the adventitious carbon in the chamber. The sum of the areas under the peaks were then used to determine relative ratio of different states.

Raman system (Renishaw inVia/Bruker Innova) was used with 514 nm illumination, which was provided by a Modu-Laser 50 mW Ar^+ ion laser. The procedure used the 10% power and five accumulation time.

The XANES and EXAFS measurements at Mo K-edges were performed at the Advanced Photon Source (APS) on the bending-magnet beamline 20-BM-B with electron energy of 7 GeV and average current of 100 mA. The radiation was monochromatized by a Si (111) double-crystal monochromator. Harmomic rejection was accomplished with 15% detune. All spectra of samples were collected in fluorescence mode by PIPS detector. For energy calibration, the first derivative peak of Mo foil was adjusted to 20000 eV. Data reduction and analysis were processed by Athena software.

Scanning electron microscopic (SEM) images were recorded with Zeiss Sigma 500 Field-emission scanning electron microscopy (FESEM) on a JEOL JSM-6700F operating at 10 kV.

The differential electrochemical mass spectrometry was built based on a purchased mass spectrometer (HPR-40, Hiden Analytical). The volumes of the cell head space, the transfer line, and the sample cross were all

calibrated by known volume tubings. The mass spectrometer was calibrated by standard mixture gas of CO_2, O_2, and H_2 (2%, 5%, and 10%) in Ar. The discharge process was performed by flowing oxygen in the cell and monitoring the oxygen consumption by pressure transducer (PX419-USBH). After discharge, all the gas leftover in the cell was tested by the mass spectrometer and no other gas was detected. Hence, we assume that only oxygen participates in the electrochemical reaction and the change of pressure is only related to the change of oxygen in the cell. The charge process was tested by injecting the gas generated from the cell every 10 min to the mass spectrometer.

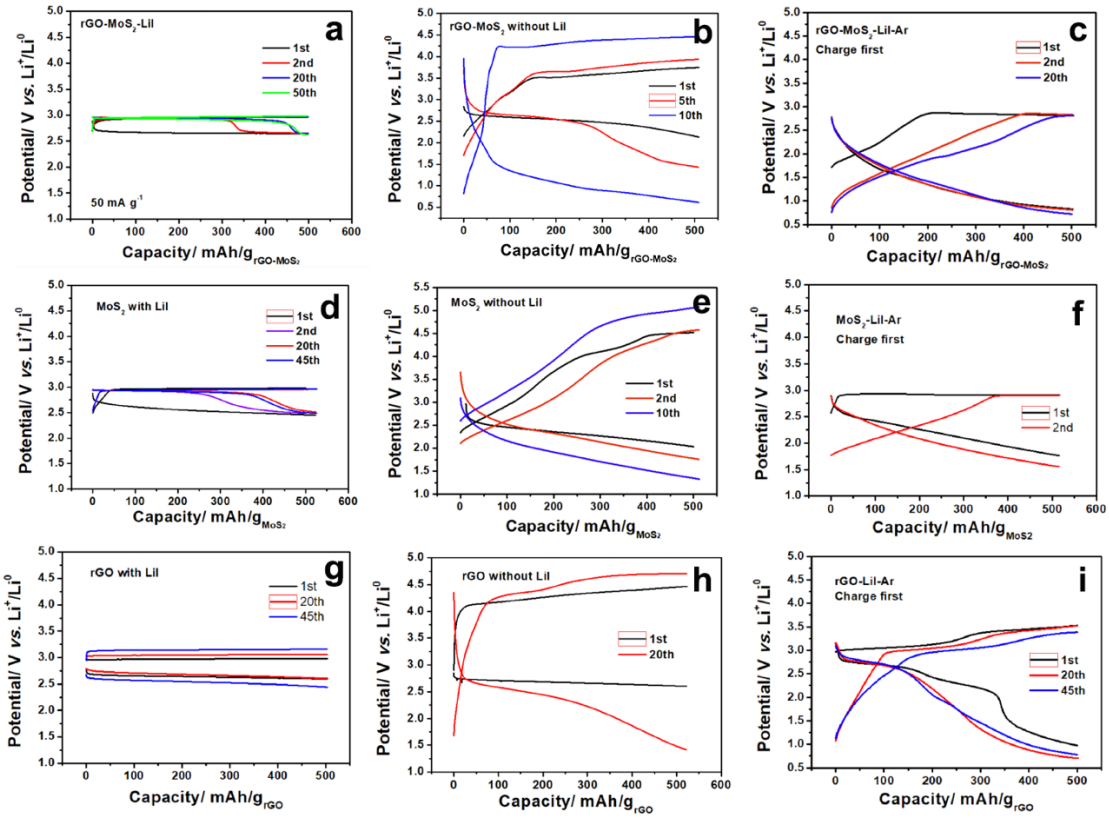

Figure S1. Potential curves of the rGO-MoS_2 (a-c), MoS_2 (d-f) and rGO (g-f) with (a, d and g)/without (b, e and h) LiI for Li-O_2 and Li-ion batteries (c, f and i): a) rGO-MoS_2 with LiI for Li-O_2 battery; b) rGO-MoS_2 without LiI for Li-O_2 battery; c) rGO-MoS_2 with LiI for Li-ion battery; d) MoS_2 with LiI for Li-O_2 battery; e) MoS_2 without LiI for Li-O_2 battery; f) MoS_2 with LiI for Li-ion battery; g) rGO with LiI for Li-O_2 battery; h) rGO without LiI for Li-O_2 battery; i) rGO with LiI for Li-ion battery;. 500 µL electrolyte and 50 mA/g current density is used in all cells. The distinctive potential curves between the rGO and MoS_2 with LiI demonstrate different reactions occur in these two cells rather than the Li-I reaction.

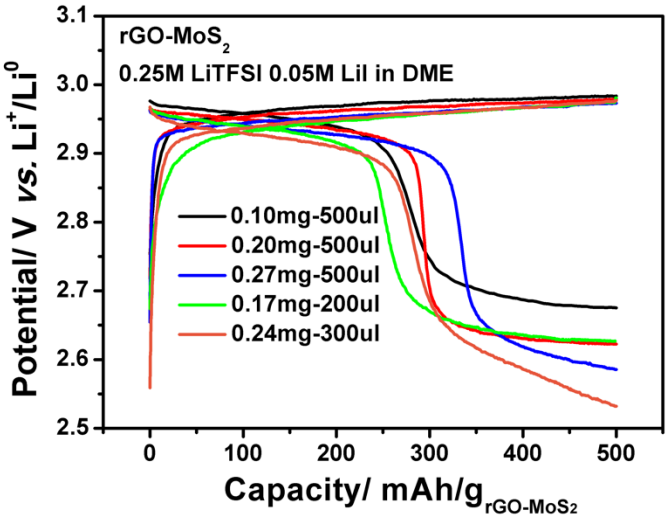

Figure S2. Potential curves of rGO-MoS_2 with different active material loading and electrolyte amount at the second cycle.

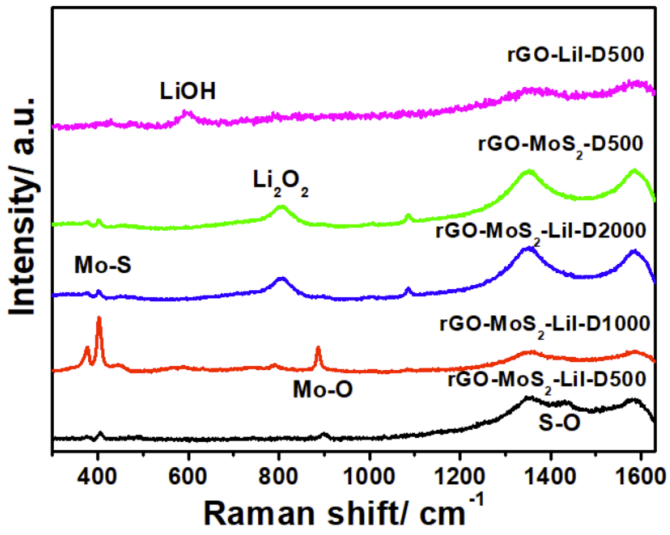

Figure S3. Raman spectra of the varied discharge samples, obtained from different conditions. After discharge to 500 mAh g^{-1}, rGo-MoS_2 with LiI forms the $Li_2MoO_2S_2$ and absence of one of them will result in LiOH and Li_2O_2. Li_2O_2 will show up and become dominated products when the rGo-MoS_2 was further discharged to 1000 and 2000 mAh g^{-1}.

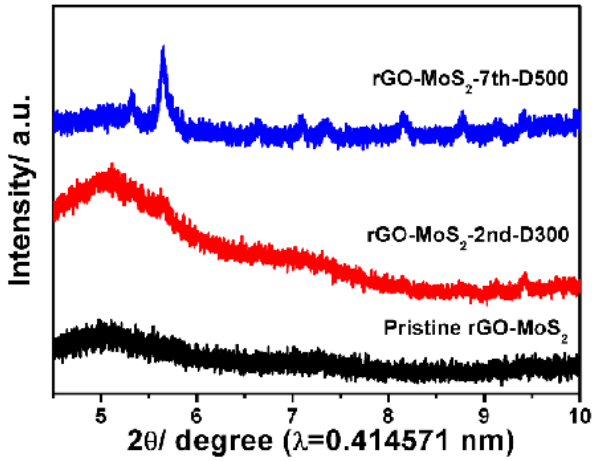

Figure S4. Synchrotron XRD results of pristine, discharged to 300 mAh g^{-1} at the 2nd cycle and discharged to 500 mAh g^{-1} at the 7th cycle rGO-MoS_2. A new set of diffraction peaks appears after discharging to 300 mAh g^{-1} at the 2nd cycle and becomes obvious after discharging to 500 mAh g^{-1} at the 7th cycle.

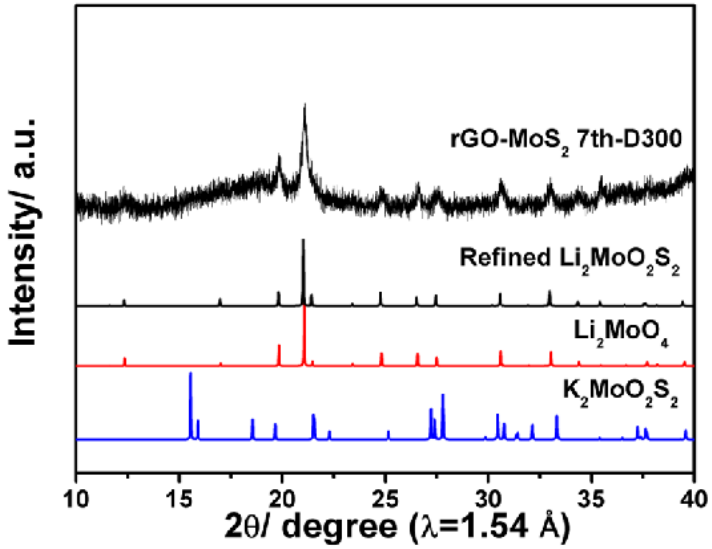

Figure S5. Compared the experimental and refined $Li_2MoO_2S_2$ patterns with the standard XRD pattern of the Li_2MoO_4 and $K_2MoO_2S_2$. The latter two patterns are from the ICSD database.

Table S1. The structure information of the $Li_2MoO_2S_2$, which is obtained by XRD refinement.

Structure 1							
Phase name			$Li_2MoO_2S_2$				
Space group			R-3H				
Cell Volume ($Å^3$)			1713.0(14)				
Wt% - Rietveld			100.000				
Crystal Density (g/cm^3)			3.5937(29)				
Lattice parameters							
a (Å)			14.3585(47)				
c (Å)			9.5939(43)				
Site	Np	x	y	z	Atom	Occ	Beq
Li1	18	0.14110	0.45500	0.25320	Li+1	1	0.0166
Li2	18	0.30900	0.85620	0.58230	Li+1	1	0.0174
Mo1	18	0.11834	0.64730	0.41611	Mo+6	1	0.01032
O1	18	0.00523	0.66467	0.41520	O-2	1.00(11)	0.0157
O2	18	0.23365	0.77686	0.41607	O-2	1.00(11)	0.0176
S1	18	0.11925	0.57890	0.26342	S	1.00(18)	0.0162
S2	18	0.11907	0.57810	0.56859	S	1.00(13)	0.0162

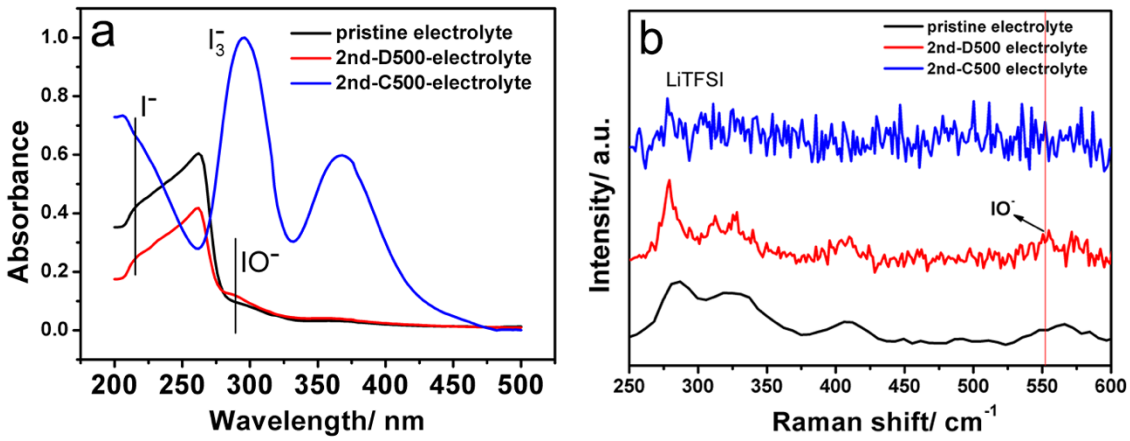

Figure S6. UV spectra (a) and Raman spectra (b) of the pristine, after 2nd discharge and charge electrolytes.

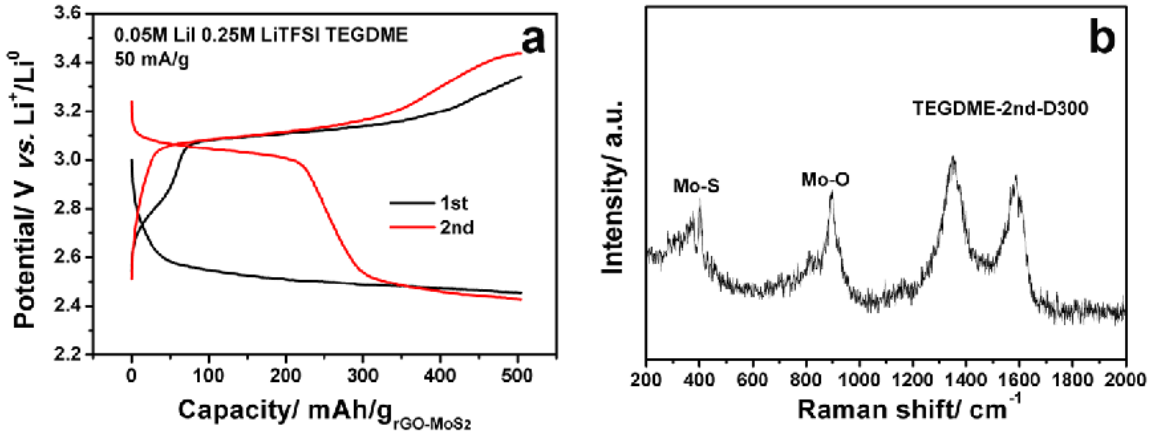

Figure S7. Potential curves (a) of rGO-MoS_2 at the first two cycles and Raman spectrum (b) of the discharged sample to 300 mAh g^{-1} at the second cycle the when TEGDME replaces the DME in the electrolyte. The results show that rGO-MoS_2 shows the similar behavior.

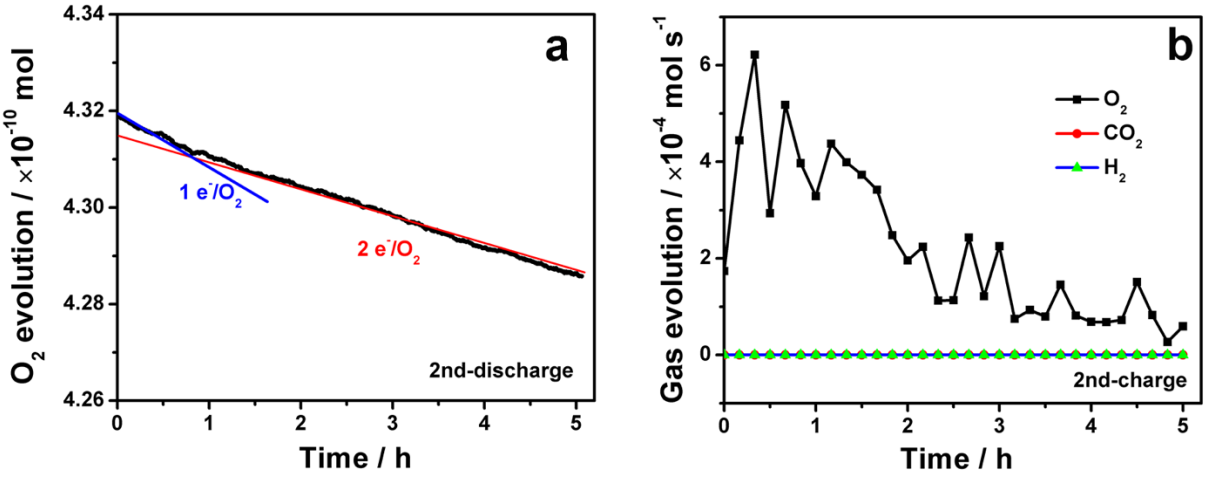

Figure S8. DEMS spectra during 2nd discharge (a) and charge (b) states.

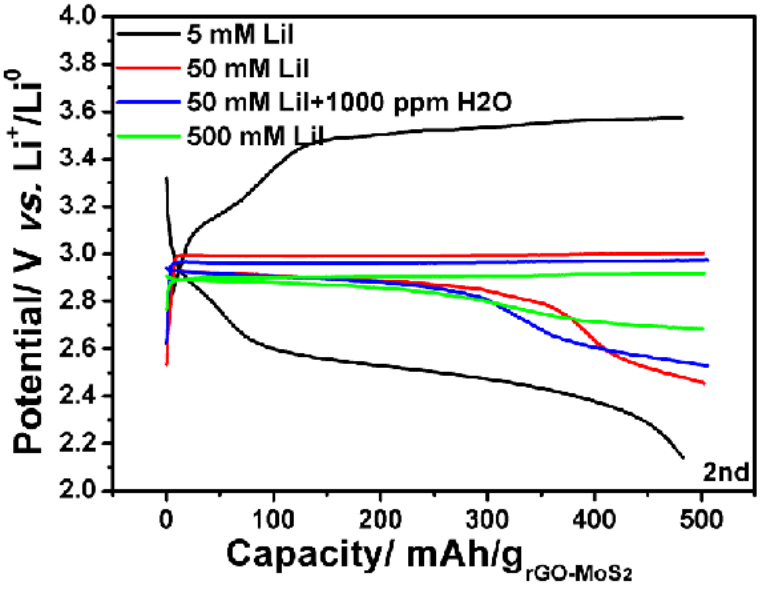

Figure S9. Potential curve of the rGO-MoS_2 at the second cycle with different concentration of LiI and H_2O in the electrolyte. Increasing the LiI and H_2O content is beneficial for reducing the polarization of the cell.

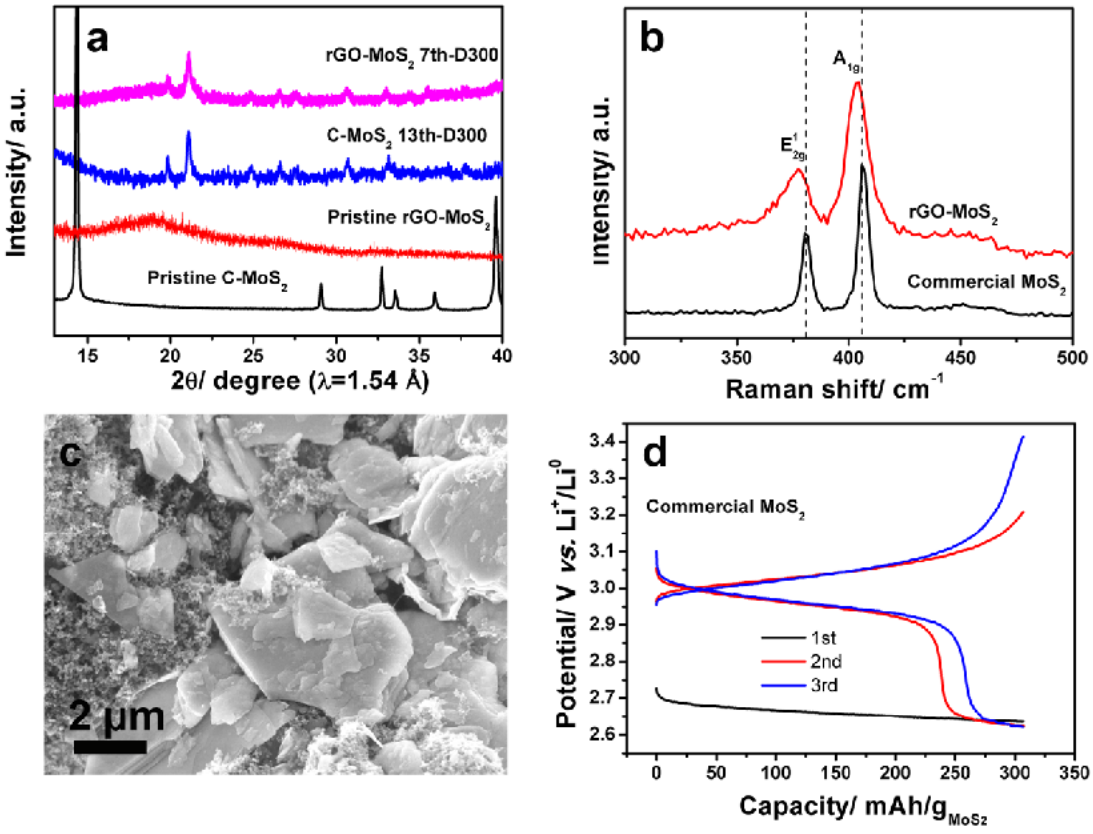

Figure S10. Feasibility of the commercial MoS_2. The compared XRD patterns (a) and Raman spectra (b) between home-made rGO-MoS_2 and commercial MoS_2, SEM images (c) and potential profiles of commercial MoS_2 electrode for Li-O_2 batteries with LiI in the electrolyte. Compared with home-made rGO-MoS_2, commercial MoS_2 is well crystallized (a) and has larger particle size (c) and narrower interlayer since its Raman peaks shift to the high wavelength (b). Nevertheless, the commercial MoS_2 exhibits the similar electrochemical behavior (d) and gets $Li_2MoO_2S_2$ as discharge product (a) of the cell.

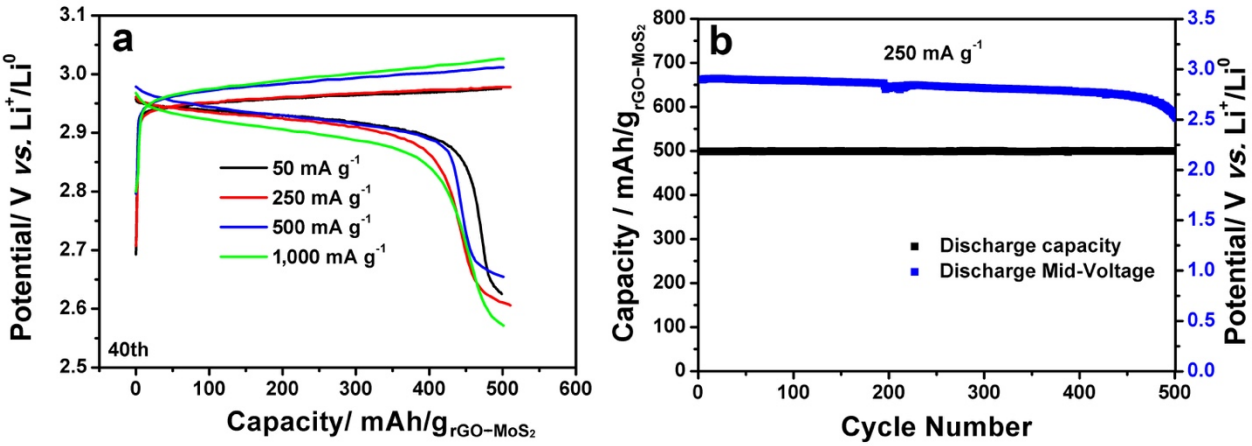

Figure S11. Rate and long cycling performance of the rGO-MoS_2 for Li-O_2 batteries with LiI. (a) The charge and discharge potential curves at the 40th cycle with the different rates. The 40th cycle is selected because most capacity is associated with the formation of $Li_{2x}MoO_{2x}S_2$. (b) The evolution of the discharge capacity and mid-voltage as a function of the cycling number at 250 mA g^{-1}.

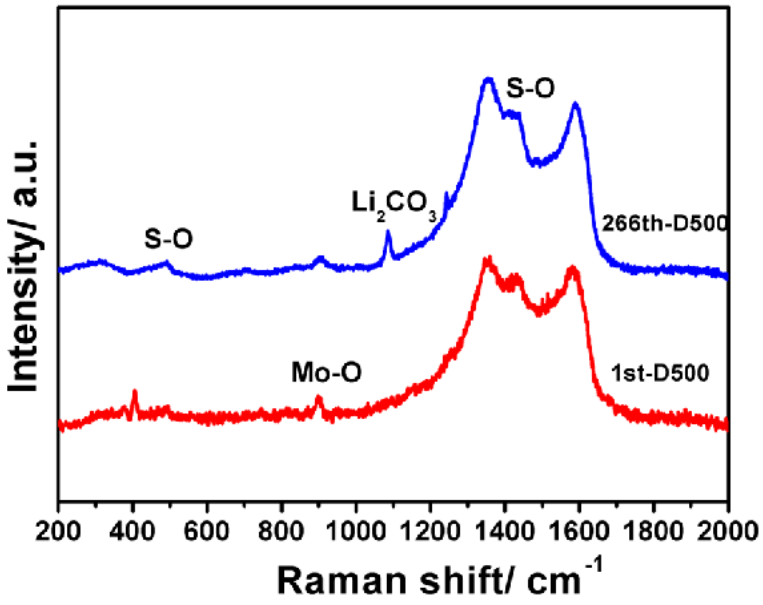

Figure S12. Compared Raman spectra of the discharge samples between 1 cycle and 266 cycles.

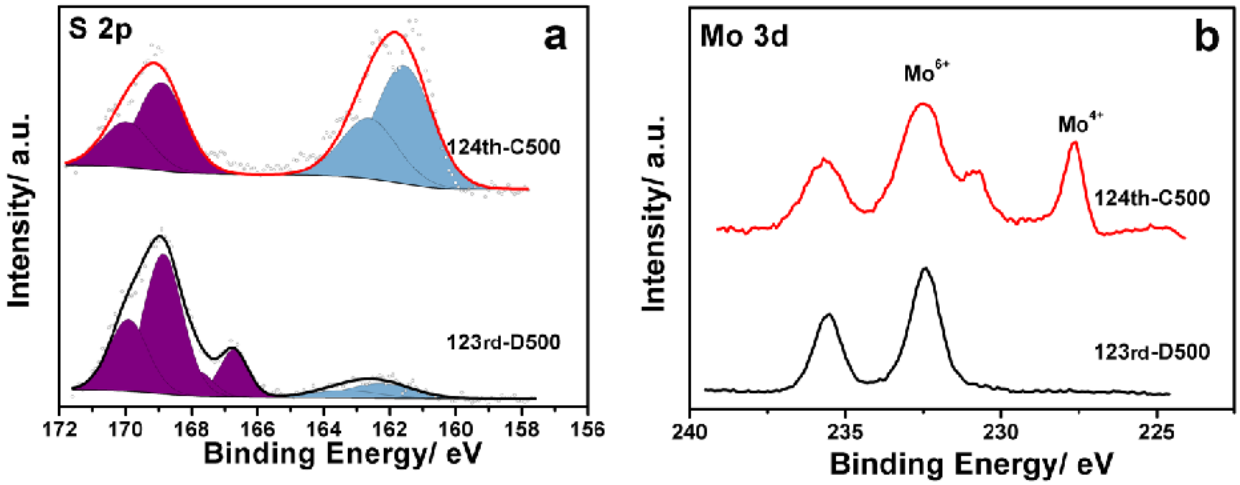

Figure S13. XPS spectra of the S 2p (a) and Mo 3d (b) at 123rd discharge and 124th charge state. After 123 cycles, MoS_2 is still responsible for the charge compensation during cycling, which is oxidized after discharge and recovered after charge.

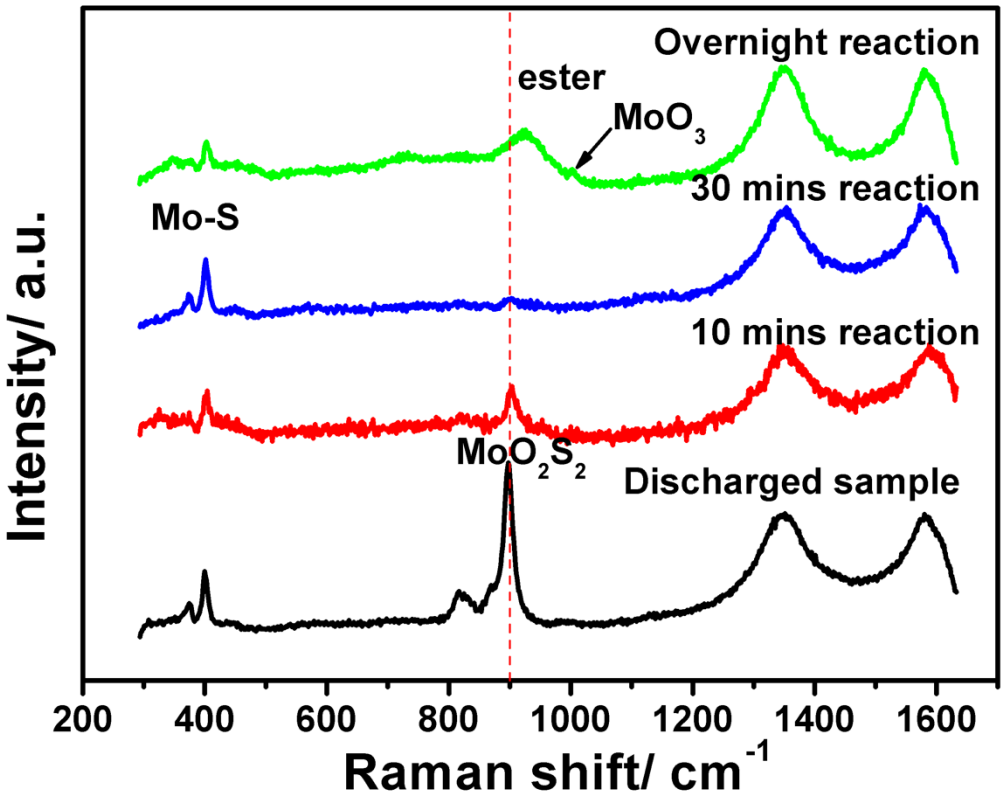

Figure S14. Raman spectra of $Li_2MoO_2S_2$ at different reaction time with 50 mM I_3^-/DME solution with 500 ppm H_2O. Overnight reaction will further oxidize the MoS_2 to MoO_3.

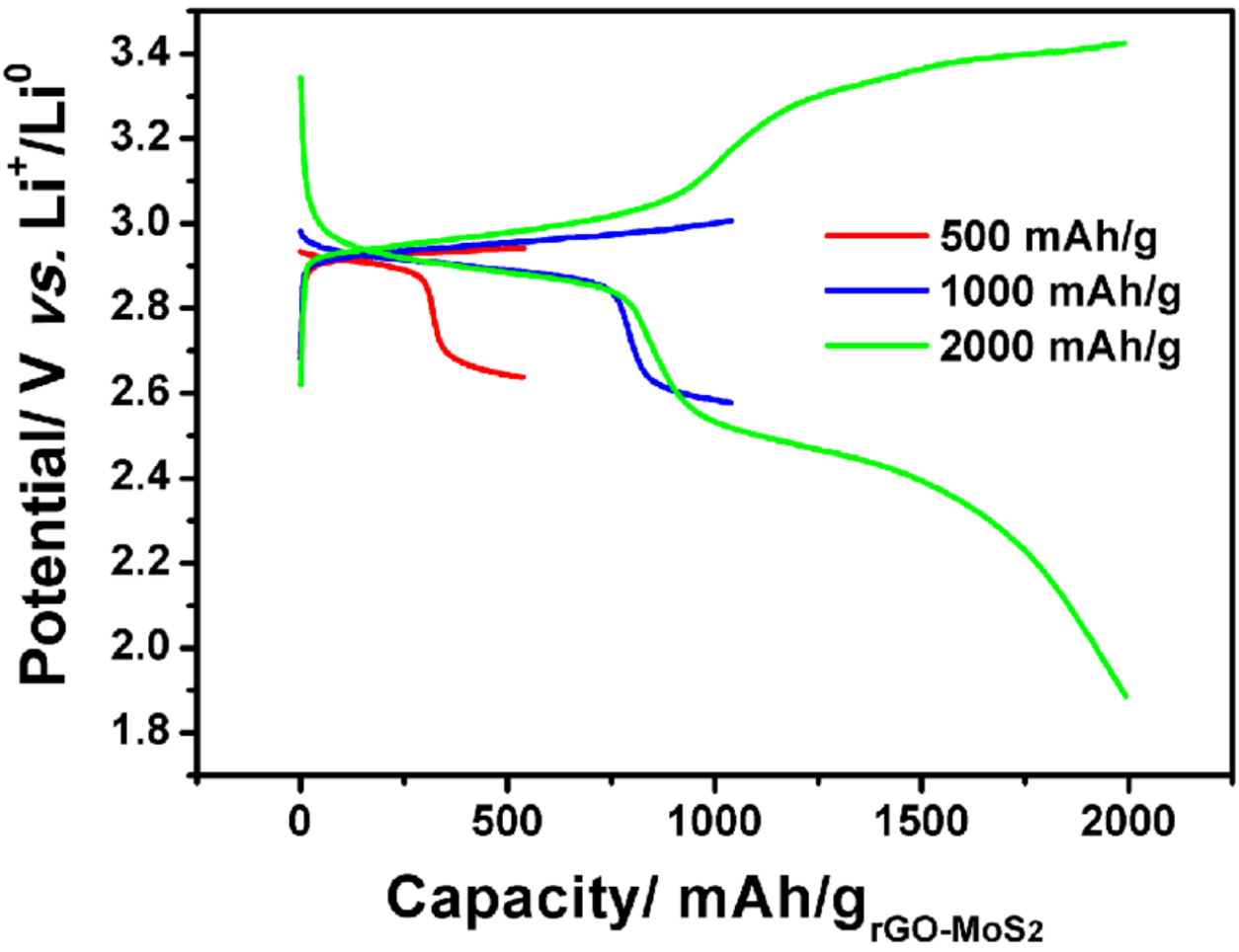

Figure S15. Limitation content of the inserted Li ions in the structure of MoS_2. The higher capacity is achieved after multiple cycles. Based on the capacity between 2.5-3.1 V, the maximum content of the inserted Li is about 6 per formula of MoS_2.

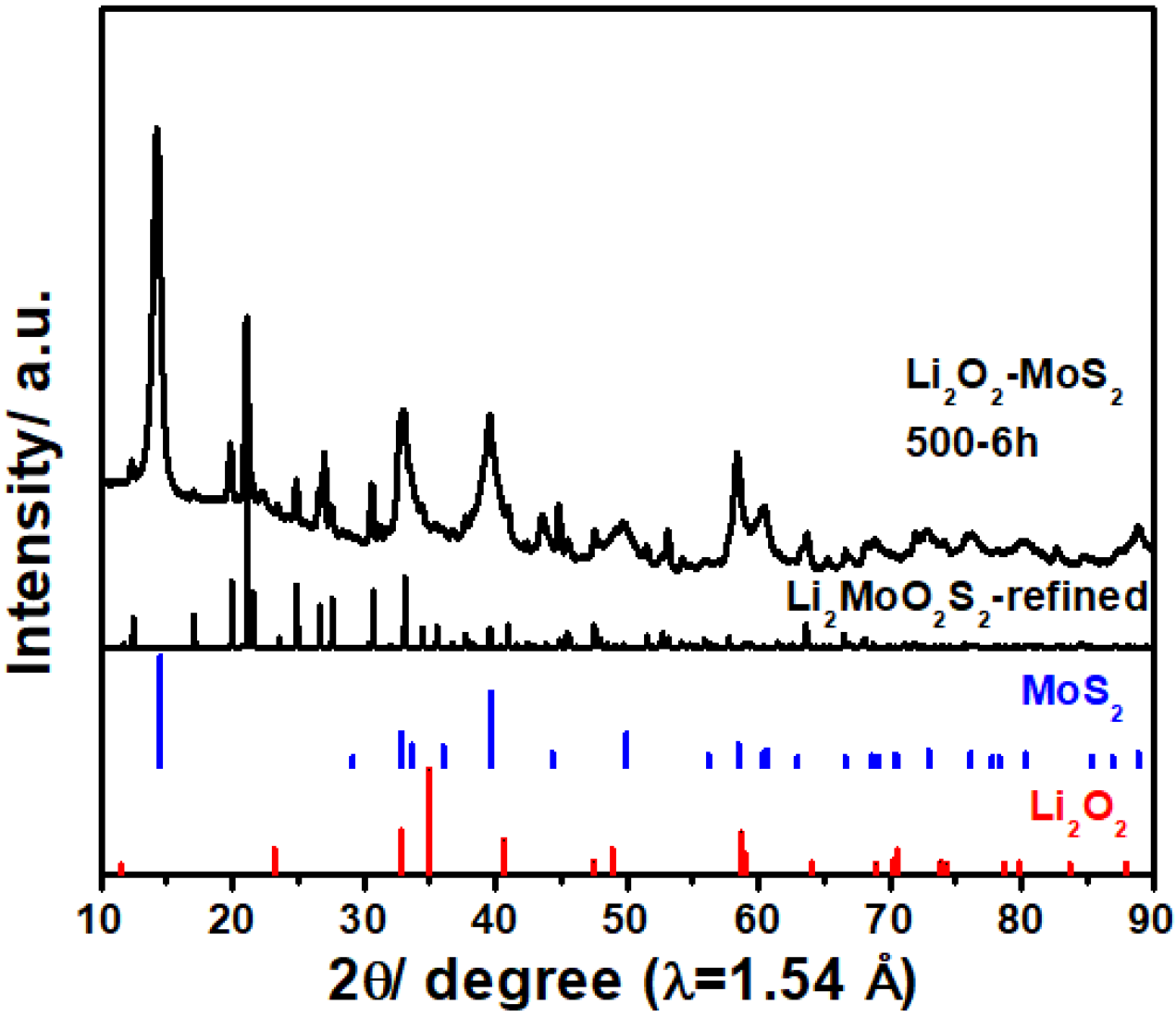

Figure S16. Compared the Li_2O_2 and MoS_2 composite after ball milling and heat-treatment and refined $Li_2MoO_2S_2$ patterns with the standard XRD pattern of the Li_2O_2 and MoS_2. The Li_2O_2 and MoS_2 composite was first ball milled at 500 rpm for 10 hours and then was heated in a sealed glass tube at 500 ℃ for 6 hours. $Li_2MoO_2S_2$ was got and more trials are needed to purify the phase.